CrystEngComm

Accepted Manuscript

ROYAL SOCIETY OF CHEMISTRY

www.rsc.org/crystengcomm

Journal Name

ARTICLE

Self-assembled hierarchical nanostructures of Bi_2WO_6 for hydrogen production and dye degradation under solar light.

Rajendra P. Panmand[a], Yogesh A. Sethi[a], Sunil R. Kadam[a], Mohaseen S. Tamboli[a],Latesh K. Nikam[a], Jalinder D Ambekar[a], Chan-JinPark[b]**,Bharat B. Kale[a]*

Three dimensional (3D) hierarchical nanostructures of orthorhombic Bi_2WO_6 with unique morphologies were successfully synthesized by solvothermal method. The precursor concentration plays key role in the architecture of hierarchical nanostructures. At higher precursor concentration, peony flower and at lower concentration RBC like morphology with average diameter 1.5µm has been obtained. These hierarchical nanostructures have been assembled by self-alignment of nanoplates of 20 nm. Having band gap in visible region, photocatalytic activity of Bi_2WO_6 hierarchical nanostructures for hydrogen production from glycerol, degradation of Rhodamine B (RhB) and Methylene Blue at ambient conditions under solar light has been investigated. The Bi_2WO_6 with penoy flower morphology was observed to be most efficient photocatalyst among (H2: 7.40 mmolh^{-1}g^{-1}, k_{RhB}:0.240 and k_{MB}: 0.100) the other reported nanostructures. The highest activity for peony flowers is due to its porous nature, high surface area and lower band gap. Such unique 3D nanostructures of Bi_2WO_6 have been architectured for the first time and their photocatalytic hydrogen production from glycerol are hitherto unattempted. These nanostructures may have good potential for ferroelectric, piezoelectric, pyroelectric and nonlinear dielectric applications.

1. Introduction

The large scale 2 and 3D self-assembly of nanostructured building block with significant morphologies and tunable properties are of great interest to researchers. The material scientists are investigating not only the properties of these assembled nanostructures but looking for their great potential for technological application.[1,2]A good progress has been made in highly organized self assemblies of metals, semiconductors, hybrid materials based on different driving mechanisms. However, it is still a great challenge to architecture such nanostructured assemblies with reliable synthesis methods. Recently, many researchers have investigated such 2 and 3D hierarchical structures for variety of applications.[3-7]Such assemblies have tremendous scope in photocatalysis because of its high surface area, optical and electronics properties. Currently, many researchers are investigating dye degradation and hydrogen production using such 2 and 3D hierarchical nanostructures. Such novel structures can be architectured by bottom up technique which requires highly tunable building blocks.

The oxide semiconductors of Aurivillius structures have an immense importance due to their layer structures and unique properties.[8] Among these semiconductors, Bi_2WO_6 is n type semiconductor and have significance because of its excellent intrinsic physico-chemical properties. Bi_2WO_6has been used as photocatalyst for Rhodamine B dye degradation by few researchers.[9-10,11(a-c)] However, very limited study was performed on shape controlled and associated photocatalytic activity of Bi_2WO_6. However, 2 and 3D assemblies of Bi_2WO_6 have not studied for hydrogen production.

In last few years, there is exhaustive research toward the development of novel hydrogen production technologies from renewable and natural assets such as water and biomass.[12-14]Our group has demonstrated hydrogen production from waste H_2S.[15-19]Among the various biomass resources of hydrogen production, glycerol ($C_3H_8O_3$) has significance because of its huge production as a waste of the processing of vegetable oil.[20] The world demand for glycerol is limited and in response to the rapid increase in global biodiesel production, crude glycerol is rapidly becoming a uneconomical waste because of its

expensive disposal. Thus, current research is focused on developing new technologies for utilization of glycerol. One promising possibility is to use glycerol as a renewable source of hydrogen. This can be possible with the use of several methods including photoinduced reforming of glycerol in the liquid phase.[21-22] There are limited reports on the hydrogen generation from decomposition of glycerol. Photocatalytic reforming of aqueous solutions of glycerol at ambient conditions has been investigated with the use of Pt/TiO_2, CuO/TiO_2 and other photocatalysts under a solar light-simulating source.[23-26]

In this context, we have architectured hierarchical peony flower/bowl/red blood cells-like Bi_2WO_6 nanostructures via a simple template-free solvothermal method for the first time. These nanostructures have been thoroughly characterized by XRD, FESEM, HRTEM, UV-Vis spectroscopy. The formation mechanism along with the effects of reaction time and precursor concentrations were also investigated. Such nanostructures of Bi_2WO_6 have been used as photocatalyst for hydrogen production from glycerol which is hitherto unattempted. Additionally, performance of rhodamine B dye degradation under visible light irradiation was also studied.

2. Experimental:

All chemicals were analytical grade and used as received without further purification. In a typical case, a 90 mL aqueous solution which marked as solution A was first prepared by dissolving 60 mmol Na_2WO_4 and 0.5 gm PVP in distilled water and then sonicate it in an ultrasonic water bath for 30 min. At the same time, 100mmol $Bi(NO_3)_3 \cdot 5H_2O$ were dissolved in the 90 mL acetic acid (CH_3COOH) by vigorous stirring, and the resulting solution is marked as solution B. The mixture of A and B solution was stirred until it become homogeneous. Then the mixture was sealed in a Teflon-lined stainless steel autoclave. The autoclave was maintained at 150 ∘C for 18 h and then cooled to room temperature naturally. The precipitate was obtained by centrifuging and sequentially washing with ethanol and distilled water for several times, followed by drying at 65 ∘C for 6 h. Finally, Nanostructured flowers/bowl/disc of Bi_2WO_6 nanostructures were obtained by adjusting experimental parameters (see table 1). The phase purity of the products was characterized by XRD using a Bruker (D8). FESEM observation was performed using a Hitachi S-4800 microscope. Transmission Electron Microscopy (TEM) images and the corresponding selected area electron diffraction (SAED) patterns were obtained on a JEOL JEM-2010 instrument. The surface area was measured using a Micromeritics (NOVA 4200e) analyzer. The nitrogen adsorption and desorption isotherms were obtained at 77 K. The Brunauer-Emmett-Teller (BET) surface area was calculated from the linear part of the BET plot. The room-temperature UV-Vis absorption spectrum was recorded on a Perkin Elmer λ-950 spectrophotometer in the wavelength range of 200-800 nm.

Table 1 Experimental parameters for synthesis of Bi_2WO_6 nanostructures.

Sample	Reaction parameters of solvothermal system	Concentration of Bi^{3+} and $(WO_4)^{2-}$
BWO-1	Temp:150ºC Time:5 hr	0.150 and 0.075 M
BWO-2	Temp:150ºC Time:18hr	0.0375 and 0.019 M
BWO-3	Temp:150ºC Time:18hr	0.075 and 0.038 M
BWO-4	Temp:150ºC Time:18hr	0.150 and 0.075 M

The apparatus used for photocatalytic experiments consists of solar light-simulating source, quartz photoreactor and an on-line analysis system. The lamp housing (Oriel) is furnished with a Xe arc lamp (Osram XBO 300 W), a set of lenses for light collection and focusing, and a water filter, which serves for the elimination of infrared radiation. The photoreactor is of cylindrical shape and its top cover has provisions for measurements of solution pH and temperature, as well as connections for inlet/outlet of the carrier gas (Argon). The gas outlet is equipped with a water-cooled condenser which does not allow vapors to escape from the reactor. The outlet of the reactor is connected to the measuring cylinder for measure and collects the gas which is further used for analysis (Gas Chromatography).

Photocatalytic activities of the samples were evaluated by the degradation of rhodamine B (RhB) and methylene blue (MB) under visible light irradiation using a same lamp as mentioned above. In each experiment, 0.1 g of the photocatalyst was added to 600mL of RhB solution (1 x 10^{-5} and 1.6x10^{-5} M, respectively). Before illumination, the suspensions were vigorously stirred in the dark for 1 h to ensure the establishment of an adsorption–desorption equilibrium between photocatalyst and dye. Then the solution was exposed to visible light irradiation. At certain intervals, a 10 mL solution was sampled and centrifuged to remove the remnant of photocatalyst. Finally, the adsorption UV-vis spectrum of the filtrates was recorded using a λ-950 (Perkin Elmer) spectrophotometer.

3. Results and Discussions

The 2 and 3D nanostructures of Bi_2WO_6 were successfully designed and synthesized by facile hydrothermal process. The effect of precursor concentration and reaction time on morphologies of Bi_2WO_6 nanostructures was studied. These nanostructures were also characterized thoroughly for phase purity and optical properties.

3.1. Structural study

All synthesized samples have been characterized by XRD for structural properties. Figure 1 shows XRD pattern of Bi_2WO_6 samples i.e. BWO-1, BWO-2, BWO-3 and BWO-4 along with standard JCPDS pattern. All bismuth tungstate samples show a unique well-crystallized phase (Figure 1) having an orthorhombic structure with lattice parameters a = 0.5457 nm, b = 1.6436 nm, and c = 0.5438 nm (JCPDS 39-0256). The relative intensity of the different diffraction peaks is altered by

the reaction conditions. Crystallinity of the Bi_2WO_6 is increased with increase in precursor concentration and time. Moreover, most of the peaks observed in the diffraction patterns are in fact a composition of several diffraction lines and hence the Scherers equation for the determination of crystallite size is hardly applicable. For the better understanding and simplicity, XRD pattern of single sample (BWO-3) is given in supporting information (SI-I).
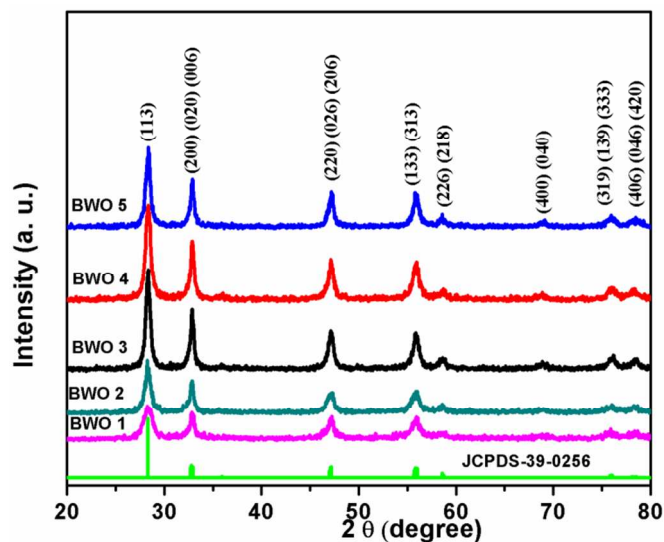

Figure 1 XRD patterns of Bi2WO6 nanostructures

3.2. Morphological study

In order to investigate the role of reaction time on morphology, controlled experiments were conducted using 0.15 M $Bi(NO_3)_3.5H_2O$ and 0.075 M $Na_2WO_4,2H_2O$ (in water and acetic acid (1:1)) at 1**50°C** for 5 hr (BWO-1) and 18 h (BWO-4).Figure 2 shows the FESEM images of the reaction time dependent morphology change of the Bi_2WO_6 nanostructures. Within a 5 h reaction time, randomly distributed nanoplates have been observed (Figure 2a). The magnified image (figure 2b) clearly shows rectangular nanoplates of size 200 x 300 nm and few nanometers in thickness. It also shows that the nanoplates are self-arranged and conferred the nanosheets (Figure 2a). This is quite obvious because at hydrothermal conditions, there is a further growth along with organization of nanoplates. Further, increase in the reaction time i.e.18 h, uniform peony flower-like hierarchical nanostructure has been obtained (Fig. 2c & d). At prolonged hydrothermal condition, strain is developed in long nanosheets which create a curvature. These curving nanosheets further self-organized to confer peony flowers of Bi_2WO_6. As discussed, each nanosheet is made up of tiny rectangular nanoeplates of average size, 200 x 300 nm (Figure 3b) and thickness 20nm. The uniform size of the peony flower has been observed (2μm).

Considering the unique flower like morphology formation at 150^0C in 18h, the further experiments were performed at various precursor concentrations under same hydrothermal conditions. Surprisingly, different morphologies are obtained by varying the precursor concentration.
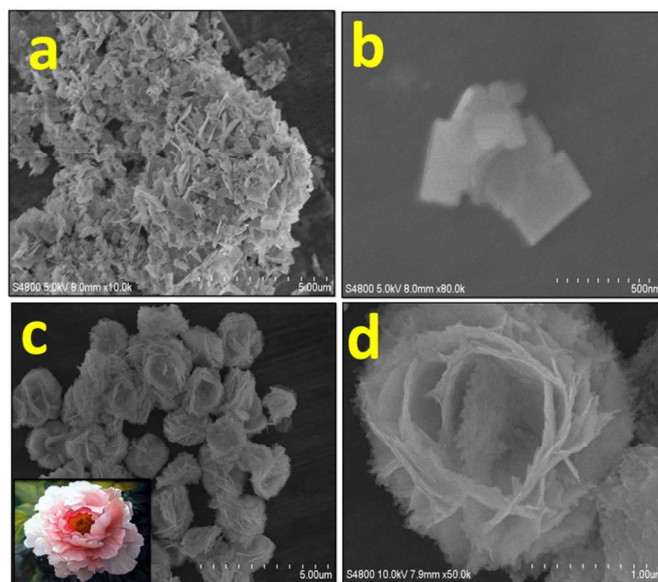

Figure2 FESEM images of the Bi_2WO_6nanostructures obtained at150^{o}C and using the concentrations of both Bi^{3+} and $(WO_4)^{2+}$ precursors0.15 and 0.075 M for 5 hr (a and b) and 18 hrs (c and d)

Figure 3 shows the FESEM images of Bi_2WO_4 obtained using different Bi^{3+} and $(WO_4)^{2+}$ precursor concentrations in water: acetic acid solution system (1:1) autoclaved at 150^oC for 18 h. Figure 3a and b show the FESEM images of uniform bowl shaped **Bi_2WO_6** nanostructures of size 1.5 μm for 0.075 and 0.038M precursor concentration of $Bi(NO_3)_3$, $5H_2O$ and Na_2WO_4, $2H_2O$, respectively (see figure 3a and b). Here, Nano plates (60 x 80 nm in width x length and 25 nm thickness) further creates nanosheets by oriental attachment. These nanosheets are much smaller as compare to previously discussed peony flower like structure. In this case,nanosheetsare not having curving nature due to smaller size. Hence, there may be seeding at the centre and peripheral growth due to orientalattachment of building blocks. The growth at the centre is slower than periphery which ultimately creates cavity at the centre. So, uniform size bowls (1.5 μm) are seen in FESEM image (Figure 3a) and magnified image shows single bowl with cavity (Figure 3b). Figure 3c and d show the FESEM images of uniform RBC shaped Bi_2WO_6 nanostructures of size 1-1.5 μm for 0.038 and 0.019 M precursor concentration of $Bi(NO_3)_3.5H_2O$ and $Na_2WO_4.2H_2O$ respectively. Surprisingly, at this concentration, FESEM image shows RBClike nanostructures of Bi_2WO_6. As discussed for both cases, the cell of 1.5 μm diameter is composed of large quantity of two dimensional nanosheets created by rectangular nanoplates of 40 x 50 nm size. These nanosheets again shows growth originated at centre and further at periphery. Hence, growth is slightly slower at centre and shows dimple at the middle which looks like RBC cell as shown in magnified image of FESEM (figure 3d). Here, again these nanosheets are stacked

by oriental attachment which is clearly revealed in FESEM image (figure 3d).

The red blood cell like structure of the Bi_2WO_6 was further investigated by TEM. Figure 4 shows images at low and high magnification of high resolution transmission electron microscopy (HRTEM) images. Figure 4a presents the HRTEM image of an individual red blood cell. The light colour at the centre indicates that the Bi_2WO_6 disc has pit in the middle, which is in accordance with the FESEM images (Figure 3h). The figure 4b is the corresponding selected area electron diffraction (SAED) pattern of the red blood cell like structure of Bi_2WO_6, which reveals its polycrystalline structure rather than well- defined single crystal.

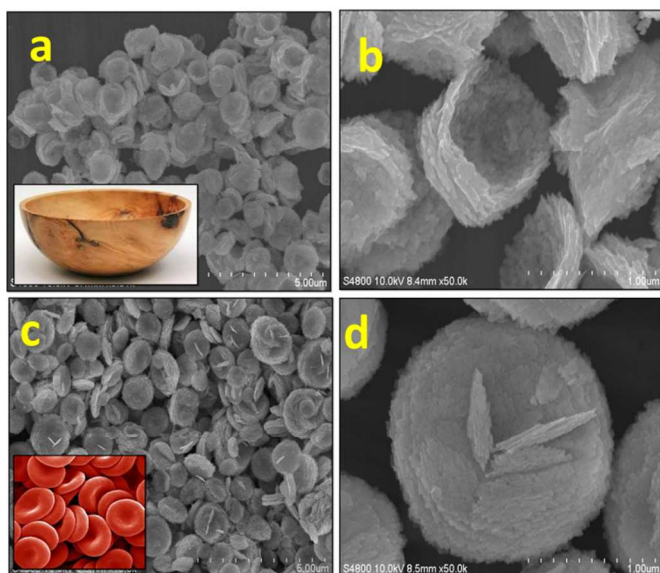Figure3FESEM images of the Bi_2WO_6nanostructures obtained at different concentrations of both Bi^{3+} and $(WO_4)^{2+}$ precursors (a,b) 0.075 and 0.0375 M, (c, d) 0.0375 and 0.01875 M

Figure 4c shows the typical HRTEM image of the edge of an individual RBC like morphology of Bi_2WO_6. Figure 4d is the magnified image of the area marked by a red rectangle in figure 4c. Figure4d clearly reveals the resolved lattice spacing of 0.272 and 0.194nm, which corresponds to the (020) and (220) plane of orthorhombic Bi_2WO_6. The observations of SAED pattern is in good agreement with XRD analysis.

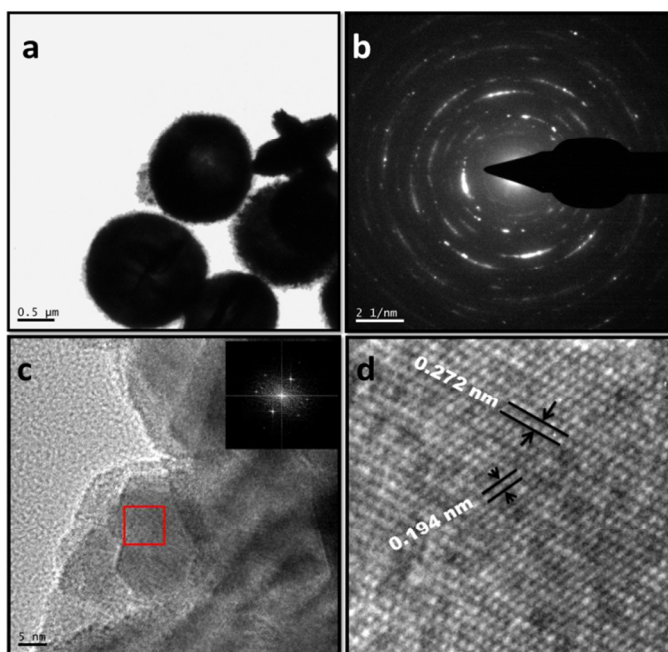Figure4HRTEM images of the Bi_2WO_6nanostructures obtained at 0.0375 and 0.01875 M concentrations of both Bi^{3+} and $(WO_4)^{2+}$ precursors. (a) Low magnified image, (b) SAED pattern, (c) HRTEM image and (d) Enlarged image of the area marked by a red rectangle in 5c.

3.3. Growth Mechanism

In the previous reports [27, 28], two main mechanisms of crystal growth are predicted for formation of flower like nanostructure. First mechanism is based on a hierarchical assembly process. In this mechanism, tiny nanoplates generally formed at the early stage and further 2D nanosheets are formed by the oriental attachment of these nanoplates. Then, the 2D sheets were self organized into 3D hierarchical nanostructures.[29,30] The second possible mechanism is through the cooperative effect of assembly and localized ripening. Initially, tiny nuclei were generated in the supersaturated solution and further growth of nanoparticles takes place with time. These newly formed nanoparticles were spontaneously aggregated to minimize their surface energy. These nanoparticles further grow anisotropically along the 2D directions, resulting in the formation of the nanoflakes. Finally, these flakes are self organized and confer the flower-like surperstructures.[9]

From morphological study by SEM and TEM analysis, it can be concluded that the formation of such intricate nanostructure is achieved via first mechanism, i.e. a hierarchical assembly process as illustrated in Figure 5. The Bi_2WO_6 tiny nanoplates may have been formed at the early stage (Figure 5B), followed by the oriental attachment of these building blocks into 2D nanosheets (Figure 5C), and finally the self-arrangement of the sheets give rise toform 3D hierarchical nanostructures (Figure 5D). In our study, the formation of primary Bi_2WO_6 nanoplates is a typical Ostwald ripening process. Initially, tiny nuclei in a supersaturated solution occurred and further formation nanoparticles by well known crystal growth phenomenon. The larger particles grew at the

cost of the smaller ones as per the Gibbs- Thomson law.[31] The further crystal growth for the formation of 2D nanostructures is strongly related to the intrinsic crystal structure of Bi_2WO_6. It has been reported that orthorhombic Bi_2WO_6 is constructed by a corner-shared WO_6 octahedral layer and $[Bi_2O_2]^{2+}$ atom layers sandwiched between WO_6 octahedral layers.[32] The layer is parallel to the (001) facets. On the basis of this structure, the chains of octahedral-W equally exist along the a- and b-axes, which indicates that the (200) and (020) faces have a much higher chemical potential in comparison with other facets.[33] As discussed previously,[28] the above feature leads faster growth rates of the (200) and (020) faces which shows preferential growth along the layer. As discussed in growth mechanism, after 5 h of reaction, Bi_2WO_6 rectangular nanoplates are formed and further 3 D nanostructure is formed due to prolonged reaction time i.e. 18 h. (See Figure 2).

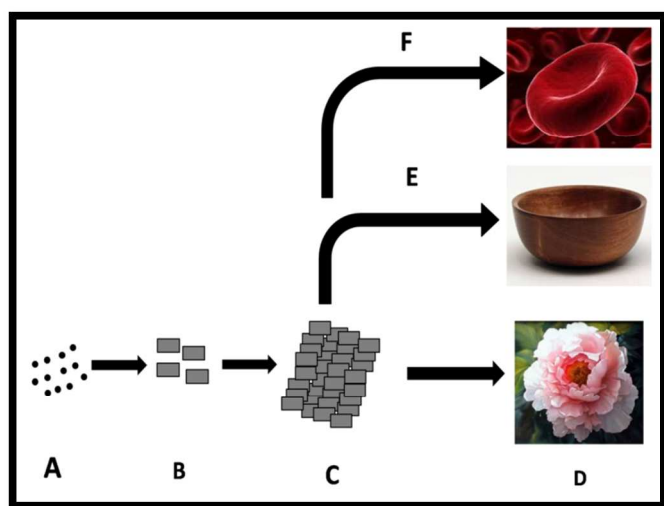Figure 5 Schematic illustration of the growth process of Bi_2WO_6 hierarchical microspheres.

In the formation of the hierarchical nanostructure via assembly process, PVP plays an important role in the formation of integrated nanosheets and multilayered structures. It is generally believed that the building blocks for oriented aggregation/attachment are usually nanoparticles with surfaces stabilized by organic coating, and weakly protected nanoparticles often undergo entropy-driven random aggregation.[34, 35] In the present work, it is believed that the selective adsorption of PVP on various crystallographic planes of Bi_2WO_6 nanoplates has significance at the initial growth stage. As evidenced by TEM and SAED results, the assembled nanosheets / layers were constructed with tiny nanoplates, with their top and lateral surfaces enclosed by (001) (020) and (220) planes, respectively. Thus, PVP should have stronger interactions with (001) planes. In contrast, it might be relatively less adsorption on (220) planes which can be removed from these crystal planes easily. This is resulting in preferential growth of assembly along the layer (a × b layer plane) rather than along the c-axis. In other words, gradual enlargements of the 2D surface areas are originating from the edge-to-edge

assembly of primary plates. With further organization of adjacent nanoplates to share the same 2D crystallographic orientation and subsequent coalescence between these building blocks confer well defined nanosheets. For the formation of 3D nanostructures, a layer-by-layer growth may be favoured(Figure 5). FESEM clearly shows formation of flat multilayered nanosheets by stacking of in-situ formed nanosheets along the [001] direction (Figure 2 a & b). This process could further reduce the surface energy of nanosheets and hence further stacking is facilitated by the special 2D geometrical shape. With a prolonged reaction time, instead of further growth of nanosheets, the existing nanosheets organized, originating from the centre which shows wrinkle. This may be acting as further template for thearchitecture of hierarchical nanostructure. This specific growth may be due to lattice tension or surface interaction in the edges of the nanosheets.[36] The such type of growth where concaveness observed along with stacking of nanosheets as it is happening in case of RBC structures. More new **tilted** nanosheets will be added into the uneven nanosheets (acting as template) which further enhance the peripheral growth and restrict at centre. Considering above mechanism, same phenomenon is applicable in case of the growth of Bi_2WO_6 nanostructures (2D flat rectangular plates, RBC like, 3D bowl like, hierarchical peony flower).

Concentration gradient (at a particular precursor concentration) under hydrothermal conditions also plays an important role in the growth of hierarchical nano-microstructure.[36,37(a), (b) & (c)] As discussed above, at lower precursor concentration, RBC like structure of Bi_2WO_6 has been observed. At lower concentration, the mobility of Bi^{3+} and $(WO_4)^-$ is slow which restrict the growth of nuclei further. Hence, very thin nanosheets are formed during reaction and at prolonged reaction time. These nanosheets are self organized with peripheral growth and create RBC like structure. The oriental attachment of nanoplates initiated via nanosheets as a seed which is placed at the centre and hence restricts the growth at the centre and favoured at the periphery. Hence, we observed the dimple at the centre in RBC structure. At slightly higher precursor concentration, bowl like morphology is observed. Due to higher concentration of precursors, mobility of ions increases which leads to augment in the growths of nanoplates. As discussed in RBC structure, peripheral growth further increases leaving slow growth at the centre. Hence, bowl like structures are observed. At further higher concentration, central as well as peripheral growthis observed. In this case, long nanosheets are formed due to higher growth rates. However, at prolonged reaction time curving nanosheets are formed due to strain developed in long nanosheets which further self-organized and form peony flower structure.

3.4. Optical properties and photocatalytic performance

The optical property of Bi_2WO_6 peony like flower, bowl and red blood cell like nanostructures was investigated by UV-Vis absorption spectroscopy (Figure 6).Tauc plot of absorption spectra is shown in inset of figure 6. It can be seen that all

Bi_2WO_6 nanostructures have a steep absorption edge in the visible range, indicating that the absorption relevant to the band gap is due to the intrinsic transition of the nanostructures.[38] The band gap (Eg) of red blood cells like morphology of Bi_2WO_6 is estimated to be about 3.06 eV from the onset of the absorption edge. This value of band gap is slightly greater than the value of peony flower (2.81 eV) like and bowl (2.91 eV) like morphology of Bi_2WO_6. The band gap widering in case of RBC structure might be due to lower particle size as compare to other nanostructures.
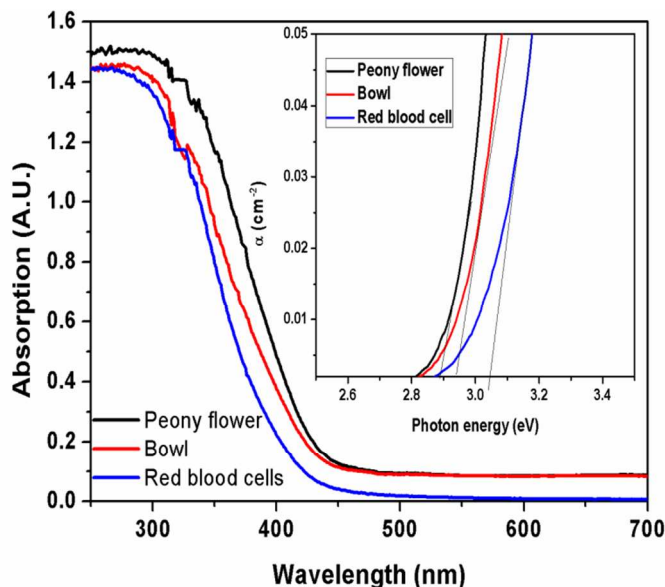

Figure 6 UV-Vis absorption spectra of peony flower, bowl and red blood cell like nanostructures of Bi_2WO_6. Inset shows the tauc plot of corresponding absorption spectra.

Photoluminescence study is useful for investigation of the migration, transfer and recombination processes of photo induced electron–hole pairs in a semiconductor because photoluminescence (PL) emission is mainly due to the recombination of these electron-hole pairs. The probability of increase in charge carrier recombination is with increase in PL intensity.[39, 40]The comparison of PL spectra (excited at 350 nm) of peony flower, bowl and RBC like Bi_2WO_6 at room temperature is shown in Figure 7. These Bi_2WO_6 hierarchical nanostructures have a broad blue-green emission peak. The intense blue emitting peaks appeared at 460 nm is associated with the intrinsic luminescence of Bi_2WO_6. This is due to the charge-transfer transitions between the hybrid orbital of Bi^{6s} and O^{2p} (VB) to the empty W^{5d} orbital (CB) in the WO_6^{2-}.[41(a)]It is well known that the doping, surface area, crystallite size and morphology affect the PL characteristics.[41 (b) & (c)]Figure 7 revealed that photoluminescence intensity of the peony flower nanostructure was quenched as compared with that of bowl and RBC like Bi_2WO_6, which clearly indicates that the recombination of photogenerated charge carriers between the hybrid orbital of Bi^{6s} and O^{2p} (VB) to the empty W^{5d} orbital is greatly inhibited by the different nanostructures. From photoluminescence study, it is confirmed that the PL intensity

decreases with increasing precursor concentration which ultimately shows the suppression of charge carrier's recombination. This could be due to different morphology with high surface area which increases surface defects. Hence, quenching of PL intensity observed in case of peony flower hierarchical structure is quite justifiable.
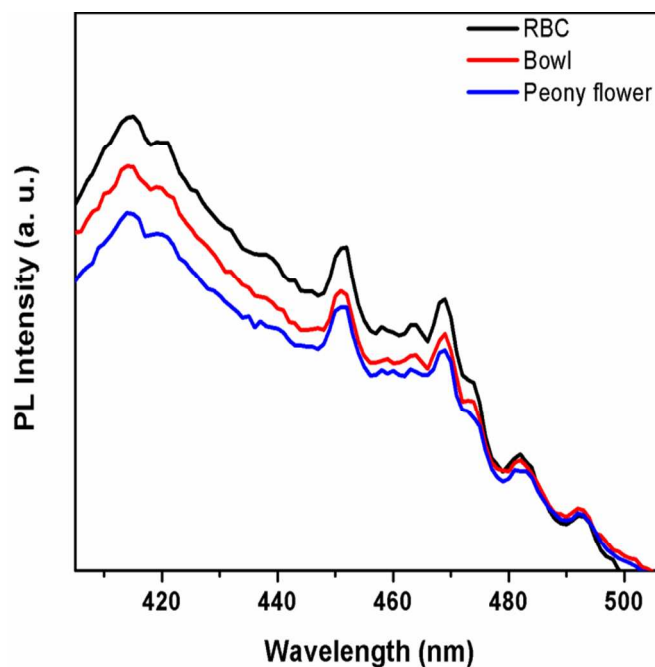

Figure 7.Room-temperature photoluminescence (PL) spectrum of the as-prepared samples (λ_{Ex}= 300 nm).

3.5. Brunauer-Emmett-Teller (BET) Analysis

Figure 8 shows the nitrogen adsorption/desorption isotherms and pore-size distribution curves (inset) of the peony flower (figure 8a), bowl (Figure 8b) and red blood cell (Figure 8c) Bi_2WO_6 nanostructures. The BET specific surface area of peony flower, bowl and red blood cell like morphology was observed to be 37.7, 33.4 and 32.1m^2g^{-1}, respectively. The inset of Figure 8 shows the Barrett-Joyner-Halenda (BJH) pore-size distribution plot for N_2 sorption isotherms of Bi_2WO_6 nanostructures. The BJH analysis showed that the resulting morphologies possessed mesopores with a mean diameter around 13.6, 14.3 and 16.3 nm for peony flower, bowl and red blood cell like morphologies, respectively (figure 8d and Table 2). The Table 2 also depicts the density of the pores whichis around 2.92 X 10^9, 2.30 X 10^9 and 1.96 X 10^9/g for peony flower, bowl and red blood cell like morphology, respectively.
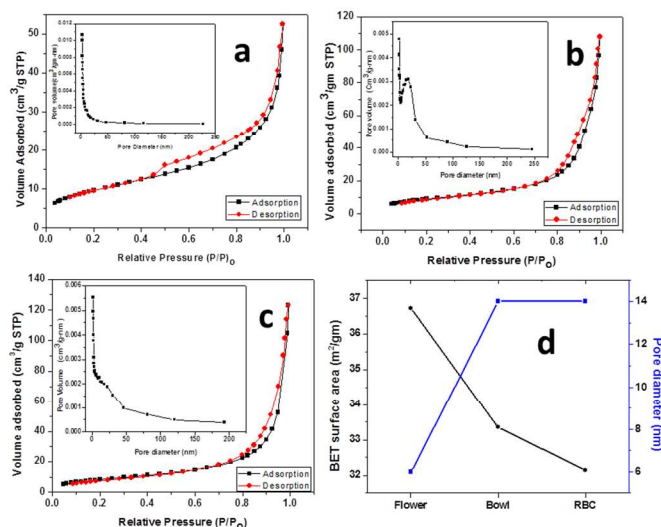
Figure 8 Nitrogen adsorption-desorption curve and pore-size distribution isotherm of peony flower (a), bowl (b) and red blood cell like morphology (c).

Table 2 Surface area and pore size distribution

Morphology	Surface area (m2/g) by BET	Pore size (nm) by BJH	Pore density (/g) X 10^9
Peony Flower	37.7	13.6	2.92
Bowl	33.4	14.3	2.30
Red blood cell	32.1	16.3	1.96

3.6. Photocatalytic Performance

3.6.1. PHOTOCATALYTIC DYE DEGRADATION

Methylene blue and Tetra-ethylated rhodamine (RhB) dyes are used in textile industries massively and hence are of the major sources of water pollution. Characteristic absorption peak of methylene blue and tetra-ethylated rhodamine (RhB) appears at around 663 and 554 nm, respectively. These absorption peaks have been used to monitor the photocatalytic degradation process.[42,43] The photodegradation efficiencies of MB and RhB mediated by the Bi_2WO_6 photocatalyst with different morphology (Red blood cell, bowl and peony flower) as well as without photocatalyst under visible-light illumination (λ> 400 nm) are displayed in Figure 9. Figure 9 also shows the $ln(C/C_0)$ as a function of time under visible light (λ>400 nm) irradiation, where C is the concentration of MB/RhB at the irradiation time t and C_0 is the concentration in the adsorption equilibrium of the photocatalysts before irradiation. The degradation rate of dyes is expressed as degradation-rate constant k which is summarized in Table 3.

Table 3 Reaction rate constant k for dye degradation

Bi_2WO_6 Catalyst	Rate constant (k)	
	MB (k_{MB})	RhB (k_{RhB})
RBC structure	0.030	0.113
Bowl structure	0.036	0.135
Peony Flower structure	0.100	0.240

Rate constant obtained for different Bi_2WO_6 nanostructures indicates that the photocatalytic performances are strongly dependent on shape, size, and structure. The peony flower like Bi_2WO_6 showed higher photocatalytic activity for the degradation of MB as well as RhB than bowl like and red blood cell like Bi_2WO_6 and as shown in Figure 9 and Table 3. The enhanced photocatalytic activity of Bi_2WO_6 hierarchical peony flower can be attributed to the combined effects of several factors: (1) the moderately high surface area of Bi_2WO_6 flower structures which ultimately enhances photo-absorption and adsorption of dye, (2) Existence of higher number of pores which can be considered as transport paths for the dye molecules on the framework walls[44] and (3) the porous peony flowers allow multiple reflections of visible light within the interior cavity which facilitates more efficient use of the light.[45]
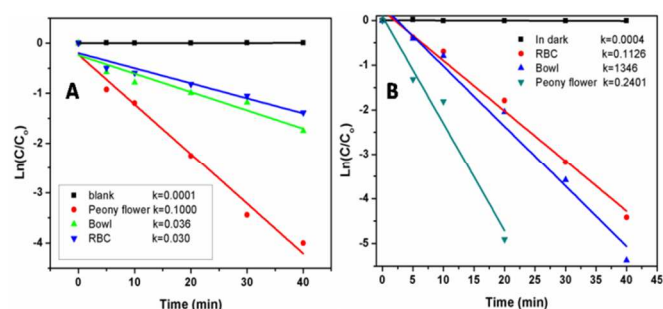

Figure 9 The effect of different catalysts on photocatalytic degradation of RhB (initial concentration 1.0 X10^{-5} M)

Figure SI-II (supporting information) reveals the temporal evolution of the absorption spectra of an MB and RhB aqueous solution catalysed by the hierarchical Bi_2WO_6 under visible light irradiation (λ>400 nm). Bi_2WO_6 is being a strong acidic oxide which has greater significance in photocatalytic dye degradation.[46] The lowering of the valance band maxima indicates that Bi_2WO_6 is having a strong oxidation power. The surface h_{vb}^+ generated in the valence band will have a stronger oxidation power. Thus, thermodynamically, OH- (or H_2O) in the solution can easily accept a part of surface h_{vb}^+ and form OH• radicals (reaction 2) which altimetry helping the oxidation of MB directly in the bulk solution. Hence, higher photocatalytic oxidation rate in the Bi_2WO_6 had been ascribed to the generation of OH• radicals.

$$OH^- + h_{vb}^+ \rightarrow OH \bullet + H^+ \quad \text{-------------------------- (2)}$$
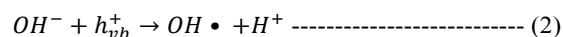
The strong absorption band of RhB located at 554 nm is due to the presence of four ethylated groups ($-C_2H_5$) attached to the

heterocyclic rings structure.[47] A regular decrease of RhB absorption under irradiation of visible light at the wavelength of 554 nm is observed, accompanied with shift in an absorption peak to lower wavelengths. This shift may be attributed to the dye's de-ethylation, i.e. from *N, N,N',N'*-tetraethylatedrhodamine to rhodamine. The intermediates formed successively presented different maximum absorption bands i.e. *N,N,N_*-triethylatedrhodamine, 539 nm; *N, N_*-diethylatedrhodamine, 522 nm; N-ethylated rhodamine, 510 nm; and rhodamine, 498 nm.[48] Also, the color of the dye solution changes from red to a light greenish yellow and then to colourless, which can be visualised normally, indicating the complete photocatalytic degradation of RhB aqueous solution during the reaction. It is reported that the mechanism of degradation of RhB is due to photocatalytic process as well as photosensitized process. In the process of degradation, Bi_2WO_6 acts as an active photocatalyst, and RhB could be degraded by direct interaction with a strong oxidizing hole originating from the hybridization of the Bi 6s and O2p orbitals.[49, 50] The RhB molecules were attacked and then degraded *via* the destruction of the conjugated structure. At the same time, in the photosensitized process, RhB dye could absorb the visible light, which was attributed to the ground state and excited state of the dye. The dye mineralization found its origin with the active oxygen radical species, O^{2-}, and the radical cations, dye$^+$. The photosensitized degradation of RhB was commonly accomplished *via* the *N*-demethylation process.[50, 51]

3.6.2.   *HYDROGEN GENERATION VIA GLYCEROL DEGRADATION.*

Photocatalytic hydrogen evolution studies are conducted over peony flower, bowl and red blood like Bi_2WO_6 catalysts from glycerol: water (1:1) mixtures under visible light irradiation. Figure 10 shows the effect of morphology on photocatalytic hydrogen evolution from glycerol and water mixture. Utmost hydrogen generation i.e. 7.4 mmoleh^{-1}g^{-1} was observed to be forthe peony flower like Bi_2WO_6 and 7.2 mmole h^{-1} g^{-1} and 4.8 mmoleh^{-1}g^{-1}for bowl like and red blood like Bi_2WO_6, respectively. The peony flower has high hydrogen evaluation rate than bowl and red blood cell like Bi_2WO_6 which may be due to the high surface area. The reason enhanced photocatalytic activity is already described in **above**section
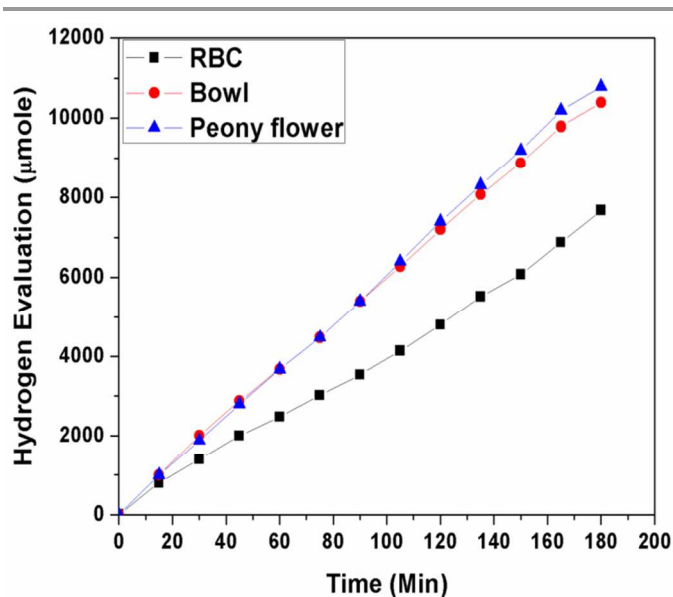

Figure 10 Hydrogen production as a function of irradiation time using Bi_2WO_6

Photocatalytic production of hydrogen from glycerol–water mixture consists of two distinct mechanisms, that is, photo-splitting of water and photo-reforming of glycerol[52]First, glycerol is oxidized, and then, it produces several intermediate compounds followed by hydrogen generation as product. Second, glycerol acts as sacrificial agent in photocatalytic water splitting[53] Glycerol, which acts as a sacrificial electron donor, is to rapidly remove the photo-generated holes (hydroxyl radicals) and/or photo-generated oxygen in an irreversible fashion, thereby suppressing electron-hole recombination and/or H_2–O_2 back reaction. By doing so, glycerol is progressively oxidized toward CO_2, with intermediate formation of partially oxidized products. When complete oxidation of glycerol (and reaction intermediates) is achieved, oxygen can no longer be removed from the photocatalyst surface and the rate of hydrogen production drops to steady-state values comparable to those obtained in the absence of glycerol in solution.

The overall process, which may be described as photo-induced reforming of glycerol at room temperature, can be expressed by the following equation.

$$C_3H_8O_3 + 3H_2O \rightarrow 3CO_2 + 7H_2 \ldots\ldots\ldots\ldots\ldots (2)$$
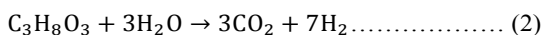
As per this reaction H_2 and CO_2 are formed after degradation of glycerol which shows that good production of hydrogen is possible. Overall, penny flowers like nanostructure of Bi_2WO_6 showed excellent Photocatalytic activity.

4.   Conclusions

In summary, we have successfully prepared peony flower, bowl, and red blood cell-like nanostructured Bi_2WO_6via a simple, rapid, economical, and efficient solvothermal process. The study showed that the PVP and precursor concentration played important role in formation of these nanostructures. The FESEM and HRTEM showed that the formation of

Bi$_2$WO$_6$architectures which is due to well-known Ostwald ripening process. The energy band structures and high BET surface areas are responsible for excellent photocatalytic activities for the degradation of MB and RhB under visible light irradiation for the peony flower, bowl, and red blood cell –like Bi$_2$WO$_6$. The peony flower likeBi$_2$WO$_6$ has showed higher photocatalytic activity for glycerol degradation for hydrogen production and other MB, RhB dye degradation than bowl and red blood cell like Bi$_2$WO$_6$. The controlled experiments showed that the morphologies affect the photocatalytic efficiency significantly due to surface defects.

5. Acknowledgements

Notes and references

*a*Centre for Materials for Electronics Technology (C-MET), Panchwati off Pashan Road, Pune-411 008, India.
*b*Department of Materials Science and Engineering, Chonnam National University, 77, Yongbongro, Bukgu, Gwangju500-757, Korea.

1. W. F. Shangguan, A. Yoshida, *J. Phys. Chem. B*, 2002, **106,** 12227.
2. R. P. Panmand,R. H. Patil,B. B. Kale, L. K. Nikam,M. V. Kulkarni,D. K. Thombre, W. N. Gade, S. W. Gosavi, *RSC Adv*.2014, **4**, 4586-4595.
3. Q. Zhang,D.Xu, X. Zhou, X. Wu, K. Zhang,*small,*2014, **10***,* 935.
4. S. Lopez-Orozco, A.Inayat, A. Schwab, T.Selvam,W.Schwieger, *Adv. Mater.***2011**, *23,* 2602.
5. J. Liu and X. W. Liu, *Adv. Mater.*2012, **24,** 4097.
6. M. Ye, H. Y. Liu,C. Lin andZ. Lin, *small*, 2013, **9,** 312.
7. Y. Li, Z. Y. Fu and B. L. Su, *Adv.Funct. Mater.*2012, **22,** 4634.
8. Y. Tsunoda, W. Sugimoto, Y. Sugahara,*Chem. Mater.*2003, **15,** 632.
9. L. Zhang, W. Wang, L. Zhou and H. Xu, *small*,2007, **3**, 1618.
10. D.N. Ke, T.Y. Peng, L. Ma, P. Cai and K. Dai, *Inorg. Chem.***2009,48***,* 4685.
11. J. Wu, F. Duan, Y. Zheng and Y.J. Xie, *J. Phys. Chem. C*,2007,**111**, 12866; (b) J. Huang, G. Tan, A. Xiao, H. Ren, L. Zang, *Res. Chem. Intermed.* 2014, **40**, 903; (b) J. A. Turner, *Science,* 2004, **305**, 972; (c)J. Zhu, J-G. Wang, Z-F. Bian, F-G Cao, G-X. Li, *Res. Chem. Intermed.* 2009, **35**, 799.
12. J. A. Turner, *Science,* 2004, **305**, 972.
13. X. Chen, C. Li, Mi. Gratzel, R. Kostecki and S. S. Mao, *Chem. Soc. Rev.* 2012, **41***,* 7909.
14. H. Tong, S. Ouyang, Y. Bi, N. Umezawa, M. Oshikiri, J. Ye, *Adv. Mater.* 2012, **24***,* 229.
15. B. B. Kale, J. O. Baeg, S. M. Lee, H. Chang, S. J. Moon, C. W. Lee, *Adv. Funct. Mater.* 2006, **16**, 1349.
16. S. K. Apte, S. N. Garaje ,G. P. Mane, A. Vinu, S. D. Naik, D. P. Amalnerkar and Bharat B. Kale, *small,* 2011, **7**, 957.
17. N. S. Chaudhari, A. P. Bhirud, R. S. Sonawane, L. K. Nikam, S. S. Warule, V. H. Rane, B. B. Kale. *Green Chem.* 2011, **13**, 2500.
18. N. S. Chaudhari, S. S. Warule, S. A. Dhanmane, M. V. Kulkarni, M. Valant and B. B. Kale, *Nanoscale*, 2013, **5,**9383
19. S. A. Mahapure, P. K. Palei, L. K. Nikam, R. P. Panmand, J. D. Ambekar, S. K. Apte, B. B. Kale, *J. Mater. Chem. A*, 2013, **1**, 2835.
20. F. Ma and M.A. Hanna, *Bioresour. Technol.* 1999, **70,** 1.
21. R. R. Davda, J. W. Shabaker, G. W. Huber, R. D. Cortright, and J. A. Dumesic, *Appl. Catal. B*, 2005, **56,** 171.
22. N. Luo, X. Fu, F. Cao, T. Xiao and P.P. Edwards, *Fuel,* 2008, **87**,3483.
23. V. M. Daskalaki, D. I. Kondarides, *Catalysis Today,* 2009*,* **144,** 75.
24. D. I. Kondarides, V. M. Daskalaki, A. Patsoura, X. E. Verykios, *Catal. Lett.* 2008, **122**, 26.
25. M. Bowker, P. R. Davies, L. S. Al-Mazroai, *Catal. Lett.* 2009, **128,** 253.
26. N. Luo, Z. Jiang, H. Shi, F. Cao, T. Xiao, P. P. Edwards, *Int. J. Hydrogen Energ,* 2009, **34**, 125.
27. D. K. Ma, S. M. Huang, W. X. Chen, S. W. Hu, F. F. Shi and K. L. Fan, *J. Phys. Chem. C,* 2009, **113**, 4369.
28. C. Zhang and Y. F. Zhu, *Chem. Mater.* 2005, **17**, 3537.
29. S. B. Betzler , A. Wisnet, B. Breitbach , C. Mitterbauer , J. Weickert , L. Schmidt-Mende, C. Scheu, *J. Mater. Chem. A*, 2014, **2**, 12005.
30. F. Amano, K. Nogami, R. Abe, B. Ohtan, *J. Phys. Chem. C* 2008, **112**, 9320–932.
31. M. Perez, *Scripta Mater.* 2005, **52***,* 709.
32. N. Kim, Rose-Noelle Vannier, C. P. Grey, *Chem. Mater.* 2005, **17**, 1952-1958.
33. S. H.Yu, B.Liu, M. S.Mo, J. H.Huang, X. M.Liu, Y. T.Qian, *Adv. Funct. Mater.* 2003, **13**, 639.
34. Z. Zhang, H. Sun, X. Shao, D. Li, H. Yu, M. Han, *Adv. Mater.* 2005, **17**, 42.
35. M. Rycenga, C. M. Cobley, J. Zeng, W. Li, C. H. Moran, Q. Zhang, D. Qin, and Y. Xia, *Chem. Rev.*, 2011, **111**, 3669..
36. Y. Li, J. Liu, X. Huang, G. Li, *Cryst. Growth & Des.* 2007, **7,** 1350.
37. (a) S. Bharathi, D. Nataraj, M. Seetha, D. Mangalaraj, N. Ponpandian, Y. Masuda, K. Senthil, K. Yong, *CrystEngComm*, 2010, **12**, 373; (b) Longzhu Zhang, Lingjun Chou, Xinheng Li, *CrystEngComm*, 2013, **15**, 10579; (c) Tierui Zhang, Wenjun Dong, Mary keeter-brewer, sanjitkonar, roland n. njabon, and z. ryantian, *j. am. chem. soc.* 2006, **128**, 10960.
38. J. W.Tang, Z. G.Zou, J. H.Ye, *J. Phys. Chem. B* 2003, **107,** 14265.
39. K. Fujihara, S. Izumi, T. Ohno, M. J. Matsumura, *Photochem. Photobiol. A: Chem.* 2000, **132**, 99−104.
40. J W, Tang Z.G.Zou and J.H.J.Ye,*J. Phys. Chem.B,* 2003, **107**, 14265.
41. (a) Q.Xiao, J.Zhang, C.Xiao, X. K. Tan,*Catal. Commun.*2008, **9,** 1247; (b) J. Liqiang, Q. Yichun, W. Baiqi, L. Shudan, J. Baojiang, Y. Libin, F. Wei, F. Honggang and S. Jiazhong, *Sol. Energy Mater. Sol. Cells*, 2006, **90**, 1773; (c) J. Wan, Z. Wang, X. Chen, L. Mu and Y. Qian, *J. Cryst. Growth*, 2005, **284,** 538.
42. Z. Liu, F. Chen, Y.Gao, Y. Liu, P. Fang, S. Wang, *J. Mater. Chem. A*, 2013, **1**, 7027.
43. G. Zhao, S. Liu, Q. Lu, and L. Song, *Ind. Eng. Chem. Res.* 2012, **51,** 10307.

44. C. Mao, M. Li, Z. Fang, F. Meng, X. Qu, Y. Liu, M. Wang, J. Zhang, Z. Shib and X. Guo, *RSC Adv.* 2013, **3,** 6631.

45. X. X. Yu, J. G. Yu, B. Cheng and M. Jaroniec, *J. Phys. Chem. C,* 2009, **113**, 17527.

46. T. Saison, N. Chemin, C. Chanéac, O. Durupthy, V. Ruaux, L. Mariey, F. Maugé, P. Beaunier, J. P. Jolivet, *J. Phys. Chem. C,* 2011, **115**, 5657.

47. S. Obregón Alfaro, A. Martínez-de la Cruz, *Applied Catalysis A: General,* 2010, **383,** 128.

48. T. Wu, G. Liu, J. Zhao, H. Hidaka, N. Serpone, *J. Phys. Chem. B,* 1998, **102**, 5845.

49. Y. Zhang, N. Zhang, Z. R. Tang and Y. J. Xu, *Chem. Sci.,* 2013, **4**, 1820.

50. H. Fu, C. Pan, W. Yao, Y. Zhu, *J. Phys. Chem. B*, 2005, **109,** 22432.

51. X. Zhao, T. Xu, W. Yao, C. Zhang, Y. Zhu, *Appl. Catal. B: Environ.* 2007, **72**, 92.

52. J. Jitputti, Y. Suzuki, S. Yoshikawa, *CatalCommun.* 2008, **9**, 1265.

53. V. Gombac, L. Sordelli,T. Montini, J. J. Delgado, A. Adamski, G. Adami, M. Cargnello, S. Bernal, P. Fornasiero; *J. Phys. Chem. A,* 2010, **114**, 3916.